Manuscript Received
4-8-85 SAR

Two-Photon Absorption, Nonlinear Refraction and Optical Limiting in Semiconductors

Eric W. Van Stryland, H. Vanherzeele, M. A. Woodall, M. J. Soileau, Arthur L. Smirl, Shekhar Guha, and Thomas F. Boggess

Center for Applied Quantum Electronics
Department of Physics
North Texas State University
Denton, Texas 76203

Two-photon absorption coefficients β_2 of eight different semiconductors with band-gap energy E_g varying between 1.4 and 3.7 eV are measured using 1.06 μm and 0.53 μm picosecond pulses. β_2 is found to scale as E_g^{-3} as predicted by theory for the samples measured. Extension of the empirical relationship between β_2 and E_g to InSb with E_g=0.2 eV also provides agreement between previously measured values and the predicted β_2. In addition the absolute values of β_2 are in excellent agreement (the average difference being <26%) with recent theory which includes the effects of nonparabolic bands. The nonlinear refraction induced in these materials is monitored and found to agree well with the assumption that the self-refraction originates from the two-photon generated free carriers. The observed self-defocusing yields an effective nonlinear index as much as two orders of magnitude larger than CS_2 for comparable irradiances. This self-defocusing in conjunction with two-photon absorption is used to construct a simple, effective optical limiter that has high transmission at low input irradiance and low transmission at high input irradiance. The device is the optical analog of a Zener diode.

Key Words: nonlinear absorption; nonlinear refraction; n_2; optical limiting; semiconductors; two-photon absorption; CdTe; GaAs; CdS; CdSe; ZnTe; ZnSe; ZnO.

1. Introduction

The ever increasing role of semiconductors in light-wave technology has created a pressing demand for the characterization of the nonlinear optical properties of these materials. Semiconductors are attractive as elements in nonlinear-optical devices because of their large and potentially extremely fast optical nonlinearities. A careful study of these macroscopic nonlinearities should allow one to determine the dependence of these nonlinearities on fundamental microscopic mechanical and electronic material properties (e.g., band gap, carrier lifetime, carrier effective mass, etc.). The data base formed by this information would then allow one to not only tabulate the materials that exhibit large nonlinearities but also to predict the specific material parameters that give rise to these high nonlinearities. This predictive capability is extremely important from the standpoint of searching for materials with large nonlinearities.

A study of the nonlinear optical properties of several semiconductors is presented here, and a relationship between the two-photon absorption coefficient (β_2) and other material properties is verified. Eight different materials were experimentally studied for which the incident photon energy $\hbar\omega$ is less than the band-gap energy E_g but greater than $E_g/2$ so that two-photon absorption (2PA) is allowed [1]. Both 1.06 and 0.53 μm picosecond pulses are used in transmission experiments using semiconductors with E_g ranging from 1.4 to 3.7 eV. We find that the 2PA coefficient β_2 is given by

$$\beta_2 = K \sqrt{E_p}\, f(2\hbar\omega/E_g)/n^2 E_g^3 \qquad (1)$$

where K is a material independent constant, n is the linear refractive index, and E_p is nearly material independent for a wide variety of semiconductors [2]. The function f, whose exact form depends on the assumed band structure, is a function only of the ratio of the photon energy $\hbar\omega$ to E_g which determines the states that are optically coupled. The scaling given by eq (1) agrees with the most recent theories for two-photon absorption [3-5] and allows for predictions of 2PA

coefficients for other materials at other wavelengths given minimal materials parameters. For example, extension of this scaling to InSb (300°K) at 10.6 μm predicts a β_2 of 6.8 cm/MW which is in excellent agreement with recent experiments. Specifically, Miller et al. [6] obtain a value of 8 cm/MW. Equation 1, is therefore valid over a range of 20 in band-gap energy from the infrared to the visible. In addition we find that the proportionality constant K as calculated by Weiler [4] for nonparabolic bands agrees with our experimentally determined K to within better than 26%.

We use the experimentally determined 2PA coefficients along with a modified Drude theory (modified to include effects of interband transitions and band filling) to model the nonlinear refraction in these semiconductors. We quantitatively fit the predictions of this theory to beam propagation data obtained for CdSe and obtain excellent agreement when all of the nonlinear refraction is assumed to arise from the carrier generation [7]. That is, the contributions proportional to the photogenerated carrier density dominate the usual bound electron nonlinear refractive index changes. This has been previously shown to be the case for one-photon absorption in materials such as InSb at 5 μm [8] and Si at 1 μm [9]. We find that the effective nonlinear refraction can be two orders of magnitude larger than that for CS_2 at comparable irradiances.

Finally we utilize the combined effects of two-photon absorption and nonlinear refraction in GaAs to make an irradiance (fluence) limiting device [10]. This device has high linear transmission at low irradiance (fluence) and low transmission at high irradiance (fluence). At very high irradiances, laser induced melting is also involved in the limiting action. This device is passive, has picosecond turn on time and is the optical equivalent of a Zener diode.

In Section 2 we describe the model used and derive the equations needed to describe both the nonlinear transmission and nonlinear refraction observed in the semiconductors studied. In Section 3 we outline the experimental procedure used to determine the two-photon absorption coefficients and present the experimentally determined 2PA coefficients. Section 4 presents a comparison of the two-photon absorption data to theory for parabolic and nonparabolic bands with and without exciton corrections. In Section 5 we present the experiments and fits to the beam propagation data using the results of Section 2. We describe a semiconductor optical limiter, based on 2PA, its design, operation, and uses in Section 6.

2. Theory

The experimental configuration used throughout this work is one in which the sample was very thin compared to the confocal beam parameter, and moreover, any self-induced beam phase changes were small enough that beam propagation effects in the sample were negligible (i.e., self action was "external" as described by Kaplan [11]). In this case the Maxwell wave equation for the propagation of the electric field E can be written as

$$2ik\ \partial E/\partial z = i\omega\sigma\mu_o\ E - (\omega^2/2c^2)\ \chi^{(3)}\ |E|^2 E \tag{2}$$

where $\chi^{(3)}$ denotes the third order nonlinear susceptibility, and

$$\sigma = (\alpha+\sigma_{ex}N)\ n\ \sqrt{\varepsilon_o/\mu_o} + i\ Ne^2/(m_{eh}\omega) \tag{3}$$

denotes the conductivity. Here, we have explicitly included the possibility of photogenerated carrier absorption through the term $\sigma_{ex}N$, where σ_{ex} is the total carrier cross section (holes + electrons) and N is the density of these carriers. Also α is the usual residual linear absorption (e.g., band tail absorption, impurity absorption, etc.), and m_{eh} is the reduced electron-hole effective mass. Writing the electric field as

$$E = Ae^{i\Phi} \tag{4}$$

with the irradiance given by $I = (n\varepsilon_o C/2)A^2$,

equation 2 can be separated giving

$$\frac{dI}{dz} = -\alpha I - \beta_2 I^2 - \sigma_{ex} N I \tag{5}$$

and

$$\frac{d\Phi}{dz} = \beta_1 I - \gamma_1 N \quad , \tag{6}$$

where β_2, the two-photon absorption coefficient, is proportional to the imaginary part of $\chi^{(3)}$ and $\beta_1 = \omega\gamma/c$ is proportional to the real part of $\chi^{(3)}$. γ is related to the more usual n_2 by $n_2(\text{esu}) = cn\gamma/40\pi$ where the right hand side of the equation is in MKS units. γ_1 in equation 6 is given by

$$\gamma_1 = \mu_o e^2 CP/(2nm_{eh}\omega) \quad . \tag{7}$$

The parameter P is introduced here to account for contributions to the nonlinear refraction proportional to N_{ex} but not explained by the Drude model. An example of such a contribution is that arising from interband transitions [12].

The equation governing the carrier generation is

$$dN/dt = \beta_2 I^2/(2\hbar\omega) \quad , \tag{8}$$

showing that for every two absorbed photons one electron-hole pair is generated. This equation is valid only for pulses short enough that recombination and diffusion can be neglected during the pulse. We assume this to be the case for our picosecond pulses [13].

We note that eq (5) for the irradiance is independent of the phase eq (6). This is due to our assumption of a thin sample (i.e., no irradiance changes due to nonlinear refraction within the material). We can, therefore, solve eq (5) simultaneously with eq (8) for the beam attenuation in a sample of thickness L. These equations must be solved numerically unless the contribution to the absorption from the photogenerated carriers is negligible. We can estimate under what conditions this is true by finding the irradiance, denoted as I_{cr}, for which the carrier absorption is equal to the multiphoton absorption. An approximate relation is found in the limit of small total absorption as

$$I_{cr} \sim 2\sqrt{2}\hbar\omega/[\sigma_{ex} t_o (1-R)] \quad , \tag{9}$$

where R is the surface reflectivity and t_o is the HW 1/e M (half-width at 1/e of the maximum in irradiance) of the assumed Gaussian temporal profile pulses. This result was first given by Bechtel and Smith [13]. Note that this critical irradiance is independent of β_2 since both the transmission change and the photogenerated carriers result from 2PA. Thus, materials with small β_2, which require high incident irradiance to observe a transmission change, will be the most likely materials to be affected by photogenerated carrier absorption.

The contribution to the change in transmission from these carriers is proportional to t_o^{-1}. Longer pulses of the same irradiance contain more energy and, therefore, produce more carriers. We can determine if these carriers are contributing to the nonlinear absorption by measuring the change in transmission for different pulsewidths. We show in Section 3 that the irradiances used are well below I_{cr} and that we can ignore photogenerated carrier absorption. This is the reason for using picosecond pulses as discussed in ref. 13. While we find the carrier absorption to be negligible, the refractive index change proportional to the carrier density eq (6) is

definitely not negligible as discussed in Section 5.

The solution to eq (5) with this assumption is

$$I(z,r,t) = (1-R)^j \, I(o,r,t) \, e^{-\alpha z}/[1+q(z,r,t)] \quad . \tag{10}$$

$$\text{where } q(z,r,t) = \beta_2 \, I(o,r,t)(1-R)(1-e^{-\alpha z})/\alpha \quad .$$

Inside the sample j=1, and behind the sample j=2, since there are two surface reflections. Also z is equal to L, the length of the sample. The effect of the rear surface reflection on the absorption has been ignored but is not expected to lead to significant errors in the determination of β_2 for the samples used [14]. Equation 10 can be rearranged to give the instantaneous transmission T' at each radial position of a sample of length L as

$$T'^{-1} = [1+q(L,r,t)] \, e^{\alpha L}/(1-R)^2 \quad . \tag{11}$$

Since q(z,r,t) is directly proportional to I(o,r,t) a plot of T'^{-1} versus incident irradiance should yield a straight line whose intercept determines α and whose slope determines β_2. Experimentally, pulses of Gaussian spatial and temporal profiles are used, which requires spatial and temporal integration of eq (10). The resulting plot of T^{-1} versus I has a slight downward curvature caused by these integrations, since at the higher irradiances both the spatial and temporal profiles are broadened toward the rear of the sample (i.e., there is more 2PA at the middle, brightest part of the beam). Taking account of the temporal and spatial integrals we find for the pulse transmission

$$T = 2\alpha(1-R)/[I_o \sqrt{\pi} \beta_2 (e^{\alpha L}-1)] \int_0^\infty dx \, \ln [1+q(L,o,o) \, e^{-x^2}] \tag{12}$$

where we have taken

$$I(o,r,t) = I_o \exp [-(r/r_o)^2 - (t/t_o)^2] \tag{13}$$

Examples of plots of T^{-1} from eq (12) as a function of I_o are shown in figures 5a and b of Section 3.

In order to model the beam profile of the pulse and its propagation, we now integrate eq (6) using eq (8) for N and eq (10) (j=1), for the irradiance to obtain an expression for the phase:

$$\Phi(L,r,t) = \Phi(o,r,t) + \frac{\beta_1}{\beta_2} (1-R) \ln [1 + q(L,r,t)]$$

$$+ \frac{(1-R)^2 \gamma_1}{2\hbar\omega \, \beta_2} \int_{-\infty}^{t} dt' \, F_1(t') \quad , \tag{14}$$

where

$$F_1(t) = \alpha \ln [1 + q(L,r,t)] - \frac{q(L,r,t)\alpha}{1-e^{-\alpha L}} \left[1 - \frac{e^{-\alpha L}}{1 + q(L,r,t)}\right]$$

Equations 10 (j=2) and 14 together, completely describe the electric field at the exit plane of the sample. From these solutions for I(L,r,t) and Φ(L,r,t), the field at any position outside the sample (L+z,r,t) can then be determined using the Huygens-Fresnel propagation formalism as [15]

$$E(L+z,r,t) = \frac{2\pi}{i\lambda z} \exp\left(\frac{i\pi r^2}{\lambda z}\right)\int_0^\infty r'dr' \; E(L,r',t - \frac{z}{c}) \exp\left(\frac{i\pi r'^2}{\lambda z}\right) J_o\left(\frac{2\pi rr'}{\lambda z}\right) . \qquad (15)$$

What we measure in our experiments, using short pulses, is the fluence given by

$$F(L+z,r) = \frac{c\varepsilon_o}{2}\int_{-\infty}^{\infty} |E(L+z,r,t)|^2 \, dt \qquad (16)$$

Experimental results are compared with numerical evaluations of eq (16) and/or spatial integrals of eq (16) as described in Section 5.

3. Experiment and Data

3.1 Experiment

In the first set of experiments we measured the transmission of several semiconductors as a function of incident irradiance to determine their nonlinear absorption coefficients. The experimental arrangement is shown in figure 1. The laser source used was a microprocessor controlled, passively mode-locked, Nd:Yag laser that produced single amplified pulses of energy up to 7 mJ per pulse at 1.06 μm when operated in the TEM_{00} mode [16]. The pulsewidth could be varied between 40 and 150 psec (FWHM) by selecting etalons of varying thickness as the output coupler. The width of each pulse was monitored by measuring the ratio, R, of the square of the energy of the fundamental (1.06 μm) pulse to the energy of the second harmonic (0.53 μm), pulse that was produced in a $LiIO_3$ crystal [17]. This ratio is directly proportional to the laser pulsewidth provided that the spatial profile remains unchanged. This ratio was calibrated by measuring the pulsewidth using nearly background free second-harmonic autocorrelation scans while accepting only pulses having a fixed ratio R within 15% of a preset value. To ensure that the ratio, R, was proportional to the pulsewidth autocorrelation, scans were performed for three output coupler etalons, and indeed, the ratio scaled properly. An example of such an autocorrelation scan is shown in figure 2 along with the best Gaussian fit. The autocorrelation width of 54 psec (FWHM) corresponds to a Gaussian pulsewidth of 38 psec (FWHM).

When 0.53 μm light was required, a temperature tuned CDA crystal was placed in the beam at the position indicated by the arrow in figure 1. Light at 1.06 μm was blocked with a polarizer and two 100% dielectric reflecting mirrors. Autocorrelation scans of the second harmonic beam performed with an angle tuned KDP crystal showed that these pulses scaled as the 1.06 μm pulsewidth divided by $\sqrt{2}$ to within 10%, as expected for Gaussian shaped pulses. Again the ratio R was held fixed, and the autocorrelation data was as clean as that shown for 1.06 μm in figure 2.

Two different pulsewidths of 40 and 150 psec were used in the transmission experiments on each sample at 1.06 μm. Since the output coupler etalons used to change the pulsewidth were optically contacted to a flat rotatable quartz plate, the beam line as well as the measured beam parameters remained fixed. (A few percent change in the beam spatial width probably caused by slight self-focusing in the amplifier was taken into account.) The relative error bars between one transmission experiment and the next, where only the pulsewidth was changed, were very small. While at high irradiances (a few GW/cm^2) we did see a small pulsewidth dependence of the transmission in some samples, this difference was consistent with values for the free carrier cross sections (10^{-17} to 10^{-18}cm^2). No pulsewidth dependence was observed at the low irradiance levels (0.5 GW/cm^2 at 1 μm) used to extract values of the 2PA coefficient. A calculation of I_{cr} from Section 2 for typical samples at 1 μm gives I_{cr} ~5 GW/cm^2 for σ_{ex}=5x10^{-18}cm^2. In fact, eq (9), considerably underestimates I_{cr}. From computer calculations, we find that I_{cr} is several times larger, the difference arising mainly from the fact that the spatial irradiance averaging was ignored in the approximate expression. In addition, at 0.5 μm the contribution of photogenerated carrier absorption will be less than at 1 μm since $\hbar\omega$ increases and σ_{ex} decreases, both leading to an increase in I_{cr}. The maximum experimental irradiance used to extract β_2 from the 0.53 μm data was, therefore, increased to 2 GW/cm^2. The above experimental considerations justify

ignoring free carrier absorption in calculating the transmitted irradiance eq (5) [13].

The spatial beam profiles in both the horizontal and vertical direction were determined by scanning a 25 μm pinhole at the position of the sample. The beam size was adjusted at the sample by using pairs of collimating lenses. In all, four different spot sizes were used for the 1.06 μm data from 0.5 mm to 1.5 mm (FWHM). At 0.53 μm the beam size used was 0.5 mm. In addition the beam profiles were monitored on a vidicon to ensure that there were no hot spots, spurious reflections, or shot-to-shot beam width fluctuations. Figure 3 shows a representative pinhole scan for a 1.06 μm beam of FWHM 1.50 mm (FWHM).

The incident energy was continuously varied using a stepping motor controlled rotating half-wave plate in combination with a fixed polarizer. This apparatus kept the polarization on the sample fixed and introduced no measurable beam walk with rotation angle. Previous experience indicates that other alternatives, for example, rotating calcite polarizers, may cause the beam to walk across the sample and across the energy monitoring detectors.

The choice of detectors, as well as the detection geometry, was also determined to be critical. As discussed in Section 5 the phase aberrations introduced on the beam by the two-photon generated free carriers cause considerable defocusing so that the beam profile at the detector varies with incident irradiance. Figure 4 shows an example of this defocusing as observed in the near field behind a sample of CdTe. As the irradiance is increased the beam broadens and breaks up as is characteristic for self-defocusing [18]. Thus, any spatial nonuniformities in the detector response can lead to errors. Indeed care must be exercised to ensure that "external" self action [19] does not result in overfilling the transmission detector--an occurrence that could result in an overestimate of β_2 [20] or result in optical limiting as discussed in Section 6. We found, however, that by using large area detectors (1 cm^2) with a measured spatial uniformity of better than 10% and placing them as close as possible to the sample (3 cm) that these effects were eliminated. The detectors were also determined to be linear over their range of use and were absolutely calibrated with respect to a pyroelectric energy monitor [21] which was in turn checked against two others. In addition, absorbing type neutral density filters placed in front of these detectors were checked to have linear trasmission over a range at least a factor of ten greater than the range used in these experiments. Filters were never used to attenuate the beam prior to the sample. In addition, spike filters transmitting only 1.06 μm (0.53 μm) were placed directly in front of the detectors to reduce optical noise from the flashlamps.

3.2 Data

Table I lists the 10 samples used in these experiments. In all, eight different materials having either a zincblende or wurtzite structure were investigated. All of the samples were II-VI materials except for GaAs which is a III-V material. The thickest sample used (0.5 cm) was over 100 times thinner than the confocal beam parameter (the Rayleigh distance) used for this study. Experiments were performed on each single crystal sample for two orthogonal directions of linear polarization. Within our experimental accuracy, no anisotropy in the measured values for β_2 was observed. A 15 percent variation was reported in ref. 34 for room temperature CdTe; however, the optical pulsewidth was not given. In addition the absolute values of the 2PA coefficients reported there were an order of magnitude larger than we measure. This may indicate the dominance of carrier absorption for long pulses. In ZnTe and the single crystal CdTe, the light propagation direction k was in the (110) direction and in GaAs, $\underset{\sim}{k}$ was in the (111) direction. In CdSe, $CdS_{.5}Se_{.5}$ and $CdS_{.25}Se_{.75}$, $\underset{\sim}{k}$ was parallel to the c axis; while in CdS and ZnO, $\underset{\sim}{k}$ was perpendicular to the c axis. Examples of data used to extract the 2PA coefficient are shown in figures 5a and 5b for 1.06 μm and 0.53 μm respectively. Each data point is the average of five laser firings. The solid line in figure 5a is a fit for CdSe using $\alpha=0$ and $\beta_2=18$ cm/GW in eq (12) of Section 2. The solid line in figure 5b is a similar fit for ZnSe using $\alpha=0.5$ cm^{-1} and $\beta_2=5.5$ cm/GW at 0.53 μm. In all samples the linear absorption was small, and its value was unimportant in the determination of β_2. In both samples of ZnS the scattering was significant and this loss mechanism was included in the model as linear absorption. In the latter case, the effect of the choice of σ on β_2 was less than 10%.

The results of these measurements of the two-photon absorption coefficients are given in the next to the last column of Table I. The absolute error bars on the values of β_2 are estimated to be ±40%. The relative error bars of β_2 determined from one sample to the next, are considerably better as observed by measuring all the samples in sequence for each spot size and each pulsewidth. For example, ZnS(y) listed in Table I always had a larger β_2 than ZnS(c). We conservatively estimate these relative error bars which are important in determining the parametric dependence of β_2 as discussed in the next section, to be ±25%.

In the second set of experiments (to be discussed in Section 5) we replaced the transmission detector in figure 1 by either a vidicon tube interfaced with an optical multichannel analyzer (PARC 1215) or by a a 25 μm pinhole placed at various radial positions and longitudinal distances from the sample. We then monitored the spatial beam profile of the transmitted beam using the vidicon, or we monitored the pinhole transmission as a function of incident irradiance. In Section 5, we describe the use of eq (16) to theoretically fit both of these results.

4. Comparison of β_2's to Theory

4.1 2PA Theory

We make three separate comparisons in this section. We first compare our experimentally determined β_2's with the theory of refs. 3, 4, and 5 using parabolic band structure. Excellent agreement is found for all materials except ZnTe. We then use the nonparabolic theory and again find good agreement for all materials except ZnTe. As shown by Weiler, [4] the differences between the parabolic and nonparabolic theories are minor so that this fit is expected. We then include exciton correction factors, as given by Lee and Fan [35] and as calculated by Weiler, [4] and we find that when these are included, ZnTe nearly fits the dependencies shown by the other materials.

As stated in ref. 5, the parametric dependence of β_2 on n, E_g and E_p was first explicitly pointed out by Pidgeon et al., [3] although it was present in the calculations of Basov et al. [36] The band structure and transition scheme used by Pidgeon et al. [3] is shown in figure 6. Calculations using this scheme have been performed for parabolic and nonparabolic bands. They found

$$\beta_2 = \frac{4\pi e^4}{\sqrt{2}m\,c^2}\,\frac{\sqrt{E_p}}{n^2E_g^3}\,f\left(\frac{2\hbar\omega}{E_g}\right) = 53.8\,\frac{\sqrt{E_p}}{n^2E_g^3}\,f\left(\frac{2\hbar\omega}{E_g}\right) \tag{17}$$

where E_p and E_g are in eV and β_2 in cm/GW in the last expression. Here, m is the electron mass, e the electron charge, c the speed of light in vacuum, and n the refractive index. The values for E_g, E_p and n for each material are listed in Table I. It is important to note that for both parabolic and nonparabolic bands the parametric dependences on n, E_g, and E_p predicted by the theories are the same. The differences lie in the function f and the ratio of $\hbar\omega$ to E_g (i.e., which states are optically coupled). Weiler [4] corrected an error in the calculation of f in ref. 3 and obtained the following expression using parabolic bands.

$$f(x) = \frac{2^5}{\sqrt{6}}\left(4+\frac{29\sqrt{2}}{12}\right)\left\{\frac{(x-1)^{3/2}}{x^5}\right\} = 96.9\left\{F_2(x)\right\} \tag{18}$$

where $F_2(x)$ is the same function defined in ref. 5. For nonparabolic bands, Weiler [4] finds

$$f_{np}^{\Delta<<E_g}(x) = \frac{32}{5}\,\frac{(x-1)^{3/2}}{x^3}\left\{\frac{3\sqrt{x}}{\left(\frac{3}{2}x-1\right)^2}+\frac{(x+1)^{3/2}}{3x^5}\,(x^4+2x^2+6)\right\}\ . \tag{19}$$

As shown in ref. 4 the differences between f_{np} for $\Delta<<E_g$ and $\Delta>>E_g$, where Δ is the split-off energy shown in figure 6 are small. The expression for $\Delta>>E_g$ is

$$f_{np}^{\Delta>>E_g}(x) = 16\sqrt{\frac{2}{3}}\,\frac{(x-1)^{3/2}}{x^3}\left\{\frac{\sqrt{x}}{\left(\frac{3}{2}x-1\right)^2}+\frac{6}{45}\,\frac{(x+1)^{3/2}}{x^5}\,\left(\frac{9}{16}x^4+\frac{5}{2}x^2+6\right)\right\} \tag{20}$$

Exciton corrections to values of β_2 have been predicted by Lee and Fan [35]. Weiler [4] has evaluated these corrections in terms of the ratio ε of the exciton binding energy E_b to the band-gap energy E_g. These ratios are listed in Table I. We reproduce the results of these calcula-

tions at the excitonic enhancement g_{ex}, of β_2, as a function of $\hbar\omega/E_g$ in figure 7 for various values of [4].

4.2 Comparison to Theory

Figure 8 shows a log-log plot of β_2 scaled by $n^2/(\sqrt{E_p}F_2)$ (see eq (10) for F_2) as a function of E_g. The solid line is a least squares fit to the data (excluding ZnTe) for a line having a slope of -3 to account for the E_g^{-3} dependence of β_2. Clearly the parametric dependences using this parabolic theory fit the data very well except for ZnTe. This single parameter fit yields a two-photon absorption coefficient given by the following equation:

$$\beta_2 = (3.1 \pm 0.5)10^3 \quad \frac{\sqrt{E_p}F_2(\frac{2\hbar\omega}{E_g})}{n^2E_g^3} \tag{21}$$

where again E_p and E_g are in eV and β_2 is in cm/GW. The values predicted from eq (21) are listed in the last column of Table I for each material. The value of the constant (3.1×10^3 in eq (21) predicted by theory from eqs. (17 and 18) is 5.21×10^3, so that the absolute values of the experimentally determined β_2's are, on the average, low by a factor of 1.7.

If we now compare the experimentally determined β_2's with the nonparabolic theory ($\Delta << E_g$, eq (19) we obtain the results shown in figure 9. While the overall fit to the parametric dependence is not quite as good as for the parabolic case (again the solid line is a least squares fit to a line of slope -3 excluding ZnTe), the absolute values are, on average, only 26% lower than predicted by this theory. The dotted line is the curve predicted by eqs. (17 and 19).

A similar plot (not shown) using eq (20) for $\Delta >> E_g$ gives an almost identical fit except in this case the difference between theory and a least squares fit of the data is reduced to only 3.5%. The actual case for these materials lies in between these two theories, although closer to $\Delta << E_g$, and may be partially responsible for scatter in the data (up to 23% change in β_2).

If we now include corrections to β_2 due to excitons as given in figure 7 we obtain the curve of figure 10. Here, we have used the parabolic theory (i.e., F_2) except for the additional scaling with g_{ex}. This correction factor has only been calculated for parabolic bands.[35] What we see in figure 10 is that most of the discrepancy between theory and experiment observed for ZnTe (g_{ex}=4.3)[4] has been removed by including excitonic enhancement. However, the overall fit to the parametric dependence (again the straight line is a least squares fit) is somewhat worse. This may be attributed to our lack of accuracy in calculating g_{ex}. Note that for most materials g_{ex} is of the order of 2 even when the coupled states are well above the gap (see fig. 7). Consequently, when excitonic enhancement is included for parabolic bands, the absolute β_2 values predicted by theory are a factor of 3.3 larger than those measured.

The reason that the exciton enhancement for ZnTe is considerably larger than for the other materials is that at 1.06 μm, two photons couple states only 3.5% above the gap, where excitonic effects should be greatest as shown in figure 7. We should point out, however, that we have only one material where the coupling is this close to the gap, and the error bars for this material are larger than for the other materials. ZnTe damaged easily allowing us to use a small spot size, only and limited the range of irradiances for fitting β_2. On the other hand (as shown in fig. 8), where there is overlap between the data taken here and data taken by Bechtel and Smith, [13] the agreement is excellent. They also obtained a large β_2 for ZnTe.

Two other data points listed in Table I and shown in figures 8, 9, and 10 require comment. The polycrystalline CdTe sample gave an experimental β_2 lower than the single crystal CdTe sample. It is designed as a 10.6 μm optical window and is doped with 10^{17}cm^{-3} indium [24]. It is not understood at present if or how these impurities lower the measured β_2. The ZnS(y) sample is a chemical-vapor-desposition grown sample that has a yellow appearance caused by crystal lattice imperfections that can be annealed out by a special heat treatment process [26]. The ZnS(c) is the same starting material that has undergone this heat treatment. It appears water clear, and its linear transmission cutoff is shifted into the UV. The indication from the data presented here is that not only has the linear absorption in the visible and near UV been reduced, but that the two-photon absorption at 0.5 μm has also been reduced by this heat treatment. That is, defects may be contributing to β_2. This may also be true for the ZnTe sample at 1 μm since it damaged easily.

5. Self-Refraction

In this section we present results for the beam propagation behind the sample given the irradiance and phase distributions of equations 10 (j=2) and 14. Equation 16 (Section II) describes the fluence at any point z,r behind the sample. We present data here using a beam of width 1.70 mm (FWHM) incident on the CdSe sample listed in Table I, that is placed near the beam waist. Thus $\Phi(o,r,t)$ is taken to be zero in eq (14). The transmitted signal was monitored at distances of 0.5 m and 2 m behind the sample which are both near field regions. Figure 11 illustrates the change in the beam profile with irradiance at z=0.5 m (using 92 psec FWHM pulses) as displayed on the vidicon. This scan is a narrow slice through the center of the beam equivalent to a pinhole scan. The dotted line is a fit to eq (16) as a function of r for β_2=18 cm/GW, P=3, and γ=0(i.e., n_2=0). We find that if present, the effects of bound electronic contributions to the nonlinear refractive index are overshadowed by the photogenerated carrier effects. This is confirmed by our other measurements which monitored the fluence transmitted by a pinhole as a function of irradiance.

Using a 25 μm diameter pinhole in front of a photodetector we measured the on-axis (r=0) fluence of the transmitted signal as a function of the peak on axis input irradiance for two pulsewidths and two distances. The results are shown in figures 12 and 13. To further verify the validity of the theory, the irradiance dependence of the transmitted fluence at an off-axis point was also measured. This is shown in figure 14.

The theoretical fits in figures 12, 13, and 14 were obtained from the numerical evaluation of F given in eq (16). Other parameters (see Table I) used in the calculation are α =.2 cm^{-1}, m_{eh}=.104 m [30]. The total density N of charge carriers generated by two-photon absorption on axis can be calculated by integration of eq (8). At a peak input irradiance of 1 GW/cm^2, we obtain a peak value of N evaluated at the input plane of the sample to be 2 x $10^{18} cm^{-3}$. We find that the best agreement between the theory and the experiments is obtained for P=3.5. The fits shown in figures 12, 13, and 14, are for values of P=3.5 ± 1, with the exact value of P adjusted between 4.5 and 2.5 to obtain the best fit. Using a two-level model, P has been calculated to be $E_g^2/(E_g^2-h^2\omega^2)$ [37]. For CdSe, E_g=1.74 eV at room temperature, and this formula predicts P=2 at 1 μm. The peak phase change undergone by the beam, calculated from eq (14) of Section II is (for I_o=1 GW/cm^2) $\Delta\Phi$ =-8.1, which is 1.3 wavelengths distortion. We have ignored the n_2 due to bound electronic effects in these calculations. Even if this nonlinearity for CdSe were as high as the n_2 of CS_2 (i.e., 10^{-11} esu), the maximum contribution to the phase change would be $40\pi LI\omega n_2/n_o$ which is 0.2 for I_o=1 GW/cm^2. This index change also would be a self-focusing effect and not a defocusing effect as observed. Thus the nonlinear refraction observed in CdSe is approximately 40 times larger than in CS_2 at this irradiance. Higher irradiances give rapidly increasing values of defocusing since the nonlinearity is induced by 2PA (i.e., a factor of two increase in irradiance gives nearly a factor of four larger phase distortion).

6. Optical Limiter

In this section we describe a nonlinear optical device (an optical power limiter) [10] which utilizes both two-photon absorption, as discussed in Sections III and IV, and the associated nonlinear refraction discussed in Section V. This completely passive device has a high transmission for low input irradiance (fluence) but it clamps the output at a constant irradiance (fluence) above a predetermined input. Such a device can be used as a protective element to restrict the irradiance (fluence) of a pulse incident upon sensitive optical components or as a regulator to smooth optical transients. This device is the optical analog of a Zener diode.

Optical limiting by nonlinear absorption in semiconductors was proposed and demonstrated in the late 1960's [38-40]. Moreover, nonlinear refraction combined with spatial filtering has been used to demonstrate optical limiting in liquid [41,42] and gas filled cells [43]. Here we demonstrate optical limiting in GaAs. Below the melting threshold, what we have done differently is to use not only nonlinear absorption (2PA) in GaAs but nonlinear refraction together with spatial filtering to construct a more effective device. Above the melting threshold, we also take advantage of a solid-to-liquid phase transition, which affects the reflectivity and transmission.

The geometry we used for optical limiting is shown in figure 15. A single 40 ps (FWHM) 1.06 μm pulse was focused to a 100 μm (FWHM) spot at the surface of the GaAs with a 465-mm-focal-length lens L_1. The transmitted beam was collected and collimated by a 381-mm-focal lens L_2 placed one focal length behind the sample. The recollimated beam then passed through a 2-mm-diameter aperture placed one focal length beyond L_2 and directly in front of a photodiode. The sample used was nearly identical to the sample listed in Table I. The limiting capabilities of the device are shown by the triangles in figure 16. At low input energies (< 0.5 μJ), the device

response was linear and was consistent with the 45% linear transmission of the GaAs and the 73% transmission of the pinhole. Above 10 μJ input, the output energy was essentially clamped at 1 μJ. The device continued to limit for input energies greater than 1 mJ. Over the full range of operation, the system transmission was reduced from 33% to 0.1%. Notice that regulation continued for input energies far above the GaAs single shot melting threshold of 0.9 J/cm^2 (indicated by the arrow in fig. 16). Above the melting threshold, the GaAs was translated before each firing so that each pulse irradiated virgin material.

Below the irradiance required for melting, as the input energy was increased, the transmission of the GaAs was reduced by 2PA. In this regime, the amplitude of the spatial beam profile transmitted by the GaAs was distorted solely by 2PA, and the phase distorted by index changes associated with the 2PA-generated free carriers as discussed in Sections II and IV. The self-diffraction associated with this phase and amplitude distortion reduced the effective pinhole transmission. Above the melting threshold, the increase in the reflectivity and absorptivity of the molten region further reduced the GaAs transmission and further distorted the amplitude profile of the transmitted beam.

The contribution of 2PA and nonlinear reflection to the limiting action can be separated from the contribution of nonlinear refraction by carefully collecting all of the transmitted energy with the pinhole removed as shown in figure 16. These results are shown by the circles in figure 16. Below E_{TH}, the nonlinear transmission is dominated by 2PA and can be fit by a 2PA coefficient of 26 cm/GW [10]. The value of 26 cm/GW reported in ref. 10 for the 2PA coefficient β_2 of GaAs is nearly identical to the value of 23 cm/GW shown in Table I and indicates the confidence in the values of β_2. These measurements of β_2 on GaAs were made independently with a nearly identical laser system. Above E_{TH}, the problem becomes much more complicated and is outside the scope of this paper. In this regime, the central region of the pulse that arrives after melting is initiated is heavily attenuated and reflected by the molten layer of GaAs. In addition, there is considerable evaporation of material for fluences more than ~10% above the melting threshold. It is clear, however, that the transition from below to above threshold is a smooth one. That is, there is no discontinuity in limiter response at threshold.

It is interesting to compare the contributions of TPA and self-diffraction just below the melting threshold. At an input energy of 80 μJ, 2PA acting alone has reduced the transmission by a factor of 5. On the other hand, the combined effects of TPA and self-diffraction have reduced the transmission by a factor of 30. Thus, the present configuration is a considerable improvement over limiters that utilize 2PA exclusively.

We should also like to contrast the present switch with the Si device demonstrated in ref. 44 that utilizes indirect absorption, free-carrier absorption, self-diffraction and a solid-to-liquid phase change to limit energetic pulses at 1 μm. The nonlinear absorption in Si at 1 μm is strictly fluence dependent, and the device operation is independent of pulsewidth for pulsewidths shorter than the carrier recombination time. The present device is considerably more complicated. The nonlinear absorption, which is dominated by 2PA, is irradiance dependent, while the nonlinear refractive index that arises from the 2PA-generated free-carriers is a time integrated effect that persists for the duration of the carrier lifetime. Nevertheless, the carriers cannot be generated without a sufficiently intense pulse, which in practice restricts this device to operation with short pulses. However, the limiting pulse energy can be varied considerably by changing the geometry (e.g., using a very short focal length lens L_1 in figure 15 will lower the limiting energy). An advantage of the present device (and 2PA-based optical limiters in general) over the Si device is its higher linear transmission at 1 m. Another more important advantage of 2PA-based limiters is the broader band-pass that they offer. For example, the GaAs device should function for wavelengths between approximately 0.9 and 1.7 μm where 2PA is the dominant absorption process.

7. Conclusion

The material parameter dependence found for a wide variety of semiconductors as discussed in Section III allows us to predict, with reasonable confidence, the two-photon absorption coefficient of other materials at other wavelengths. This includes, for example, mixed ternary compounds. Thus the 2PA at a particular wavelength can be tailored for a specific application.

The fact that this scaling fits the data so well implies that all of the important materials parameters have been included in the theory and that other contributions to β_2 (e.g., higher bands) cause small effects. One possible deviation from the predicted scaling is the effect of excitons. We have one material (ZnTe) which indicates that such effects may be important. If we attempt to extend this theory into the UV, we find that the predictions are in general considerably lower than experiments; however, a general trend can be found. If the coupled states

are well above the gap the deviations are relatively small, on the order of a factor of 4 or 5. As the coupled states get close to the gap, however, the deviation increases rapidly. For example, in RbI at 266 nm where $2\hbar\omega/E_g=1.47$ the experimentally measured 2PA coefficient of 2.49 cm/GW [45] is 3.7 times larger than predicted by eq (21). At a wavelength of 355 nm where $2\hbar\omega/E_g=1.10$, however, the measured 2PA coefficient of 5.08 cm/GW [45] is 14 times larger than predicted. This trend is maintained for the limited data available [45]. Considering color centers as excitons with large binding energies, such large correction factors may be accounted for. The role of excitons and color centers in 2PA needs further study. A study of the wavelength dependence of 2PA near the gap using a continuously tunable laser should help clarify the role of excitons.

It is interesting to look at the history of the measurement of 2PA coefficients. Figure 17 shows experimental values of β_2 reported for GaAs and CdSe for years beginning with 1966. This figure illustrates the fairly steady decrease in reported values as both the lasers and the experimental technique were refined. Much of the earlier data was obtained with nanosecond pulsed lasers where photogenerated carrier absorption is expected to dominate. Additionally in some instances multimode lasers were used. An additional experimental problem not previously recognized that can lead to an overestimate of β_2 is that the extreme defocusing present may allow some of the transmitted light to go undetected.

While this defocusing may be an experimental difficulty in determining β_2 it can be extremely useful for nonlinear optical devices such as the limiter discussed in Section VI. We found that this defocusing was quantitatively explained by attributing all of the nonlinear refraction to the build-up of excited carriers although the simple Drude theory had to be modified to allow for interband transitions. These fits indicate that interband transitions may actually dominate the refractive index change in these two-photon absorbers. In addition, we demonstrated a simple but effective optical limiter based on two-photon absorption, the associated self-defocusing, and spatial filtering. By choosing a substance with the proper materials parameters and a specific geometry, this limiting can be tailored to suit a specific need. Clearly further applications of the combined action of 2PA and self-refraction in nonlinear optical devices have and will be made.

The authors are most grateful to B. S. Wherrett for many valuable discussions concerning the theory of 2PA. This research was supported with funds from the National Science Foundation (ECS #8310625), the Office of Naval Research, the Defense Advanced Research Projects Agency, and The Robert A. Welch Foundation.

8. References

[1] E. W. Van Stryland, H. Vanherzeele, M. A. Woodall, and M. J. Soileau, in "Laser Induced Damage in Optical Materials," NBS Special Publication, to be published in 1985.

[2] $E_p=2P^2m/\hbar^2$ where P is the Kane momentum parameter and m is the electron mass, E. O. Kane, J. Chem. Phys. Solids 1, 249, 1957.

[3] C. R. Pidgeon, B. S. Wherrett, A. M. Johnston, J. Dempsey, and A. Miller, Phys. Rev. Lett. 42, 1785, 1979.

[4] M. Weiler, Solid State Commun. 39, 937, 1981.

[5] B. S. Wherrett, JOSA B 1, 67, 1984.

[6] A. Miller, A. Johnston, J. Dempsey, J. Smith, C. R. Pidgeon, and G. D. Holah, J. Phys. C Solid State Phys. 12, 4839, 1979.

[7] Shekhar Guha, E. W. Van Stryland, and M. J. Soileau, to be published, 1985.

[8] D. A. B. Miller, S. D. Smith, and B. S. Wherrett, Opt. Commun. 35, 221, 1980.

[9] H. J. Eichler, Opt. Commun. 45, 62, 1983.

[10] T. F. Boggess, A. L. Smirl, S. C. Moss, I. W. Boyd, and E. W. Van Stryland, to be published in IEEE JQE, 1985.

[11] S. A. Akhmanov, R. V. Khokhlov, and A. P. Subhorukov, "Laser Handbook," ed. by F. T. Arecci

and E. O. Scholz-Duboie, North Holland Pub. Co., Amsterdam, 1972.

[12] B. S. Wherrett and N. A. Higgins, Proc. R. Soc. Land. A379, 67, 1982.

[13] J. H. Bechtel and W. L. Smith, Phys. Rev. B 13, 3515, 1976.

[14] A. F. Stewart, "Intensity Dependent Absorption in Semiconductors," dissertation, University of Southern California, unpublished, 1980.

[15] M. Born and E. Wolf, "Principles of Optics," 5th edition, page 383, Pergamon Press, Oxford, U.K., 1975.

[16] Quantel Model YG40, Quantel International, Inc., 385 Reed Street, Santa Clara, California 95050.

[17] W. H. Glenn and M. J. Brienza, Appl. Phys. Lett. 10, 221, 1967.

[18] D. Weaire, B. S. Wherrett, D. A. B. Miller, and S. D. Smith, Opt. Lett. 4, 331, 1979.

[19] A. E. Kaplan, Radiophys. Quantum Electron. 12, 692, 1969.

[20] E. W. Van Stryland, M. A. Woodall, W. E. Williams, and M. J. Soileau, in "Laser Induced Damage in Optical Materials," NBS Special Publication #638, 589, 1981.

[21] Gentec ED-100, Gentec Inc., 2625 Dalton Street, Ste-Foy, Quebec, Canada G1P3S9.

[22] Values taken from E. O. Kane "Band Structure of Narrow Gap Semiconductors," in Narrow Gap Semiconductors Physics and Applications, ed. W. Zawadzki, Springer Verlag, New York, 1980, p. 13, for values not listed in this reference the value of 21 eV was assumed.

[23] Cleveland Crystals, P.O. Box 17157, Euclid, Ohio 44117.

[24] II-VI, Inc., Saxonburg Blvd., Saxonburg, PA 16056.

[25] Morgan Semiconductors, 2623 National Circle, Garland, Texas 75041.

[26] CVD Inc., 35 Industrial Parkway, Woburn, MA 01801.

[27] Raytheon Co., Missile Systems Div., Hartwell Rd., Bedford, MA 01730.

[28] Atomergic Chemetals, 100 Fairchild Ave., Plainview, NY 11803.

[29] Landolt-Bornstein Numerical Data and Functional Relationships in Science and Technology, Vol. 17, Semiconductors, Subvolumes (a) and (b), editor in chief, K. H. Helelwege, Springer-Verlag, New York, 1982.

[30] M. Neuberger, "II-VI Semiconducting Compound Tables," Electronic Properties Information Center, Hughes Aircraft Co., Culver City, CA, 1969.

[31] Y. S. Park and D. C. Reynolds, Phys. Rev. 132(6), 2450, 1963.

[32] These values obtained by linear extrapolation as a function of composition between the known values for CdS and CdSe. Y. S. Park and D. C. Reynolds, Phys. Rev. 132, 2450, 1963.

[33] Richard H. Bube, Photoconductivity of Solids, John Wiley & Sons, New York, New York, 1960.

[34] Stephen J. Bepko, Phys. Rev. B 12, 669, 1975.

[35] C. C. Lee and H. Y. Fan, Phys. Rev. B 9, 3502, 1974.

[36] N. G. Basov, A. Z. Grasyuk, I. G. Zubarev, V. A. Katulin, and O. N. Krokhin, Sov. Phys. JETP 23, 366, 1966.

[37] R. K. Jain and M. B. Klein, in "Optical Phase Conjugation," ed. R. A. Fisher, Academic Press, New York, 1983.

[38] J. E. Geusic, S. Singh, D. W. Tipping, and T. C. Rich, Phys. Rev. Lett. 19, 1126, 1967.

[39] J. M. Ralston and R. K. Chang, Appl. Phys. Lett. 15, 164, 1969.

[40] V. V. Arsen'ev, V. S. Dneprovskii, D. N. Klyshke, and A. N. Penin, Sov. Phys. JETP 29, 413, 1969.

[41] R. C. C. Leite, S. P. S. Porto, and T. C. Damen, Appl. Phys. Lett. 10, 100, 1967.

[42] M. J. Soileau, W. E. Williams, and E. W. Van Stryland, IEEE J. Quantum Electron. QE-19, 731, 1983.

[43] J. E. Bjorkholm, P. W. Smith, W. J. Tomlinson, and A. E. Kaplan, Opt. Lett. 6, 345, 1981.

[44] T. F. Boggess, S. C. Moss, I. W. Boyd, and A. L. Smirl, Opt. Lett. 9, 291, 1984.

[45] P. Liu, W. L. Smith, H. Lotem, J. H. Bechtel, and N. Bloembergen, Phys. Rev. B 17, 4620, 1978.

[46] S. Jayaraman and C. H. Lee, Appl. Phys. Lett. 20, 392, 1972.

[47] Ya. A. Oksman, A. A. Semenov, V. N. Smirnov, and O. M. Smirnov, Sov. Phys. Semicond. 6, 629, 1972.

[48] A. Z. Grasyuk, I. G. Zubarev, V. V. Lobko, Yu. A. Matreets, A. B. Mirnov, and O. B. Fhatberashvili, Sov. Phys. JETP Lett. 17, 416, 1973.

[49] D. A. Kleinman, Robert C. Miller, and W. A. Nordland, Appl. Phys. Lett. 23 243, 1973.

[50] Haim Lotem, J. H. Bechtel, and W. L. Smith, Appl. Phys. Lett. 28, 389, 1976.

[51] A. Saissy, A. Azema, J. Botineau, and F. Gires, Appl. Phys. 15, 99, 1978.

[52] B. Bosacchi, J. S. Bessey, and F. C. Jain, J. Appl. Phys. 49, 4609, 1978.

[53] F. Bryuknar, V. S. Vneprovskii, and V. U. Khattatov, Sov. JQE 4, 749, 1974.

[54] Michael Bass, E. W. Van Stryland, and A. F. Stewart, Appl. Phys. Lett. 34, 142, 1979.

Two-photon Absorption: λ = 1.06μm $2\hbar\omega$ = 2.34 eV

Material	form[a]	n(λ)	Eg(eV)	$E_p^{(b)}$(eV)	E_b/E_g	$\beta_2^{exp}(\frac{cm}{GW})$	$\beta_2^{theor.}(\frac{cm}{GW})$
ZnTe[c]	Z	2.79[c]	2.26[i]	19.1	0.004[o]	4.5	0.89
CdSe[c]	W	2.56[c]	1.74[j]	21	0.007[i]	18	18.6
CdTe[d]	Z	2.84[c]	1.44[c]	20.7	0.003[o]	22	25.1
CdTe[d]	Zp	2.84[c]	1.44[c]	20.7	0.003[o]	15	25.1
$CdS_{.5}Se_{.5}$[c]	W	2.45[l]	1.93[k]	21	0.010[l]	10	12.1
$CdS_{.25}Se_{.75}$[c]	W	2.51[l]	1.78[k]	21	0.008[l]	15	17.7
GaAs[e]	Z	3.43[i]	1.42[i]	25.7	0.003[o]	23	19.7

Two-photon Absorption: λ = 0.53μm $2\hbar\omega$ = 4.68 eV

Material	form	n(λ)	Eg(eV)	Ep(eV)	E_b/E_g	$\beta_2^{exp}(\frac{cm}{Gw})$	$\beta_2^{theor.}(\frac{cm}{GW})$
ZnS[f]	Zp(c)	2.40[i]	3.66[i]	20.4	0.010[i]	2.0	2.10
ZnS[f]	Zp(y)	2.40[i]	3.66[i]	20.4	0.010[i]	3.5	2.10
ZnSe[g]	Zp	2.70[i]	2.67[i]	24.2	0.008[o]	5.5	4.27
CdS[c]	W	2.60[i]	2.42[c]	21	0.012[i]	5.5	4.87
ZnO[h]	W	2.05[i]	3.20[n]	21	0.020[i]	5.0	4.77

Table 1. Material parameters and two-photon absorption coefficients of the materials studied.

(a) z=zincblende, w=wurtzite p=polycrystalline
(b) ref. 22
(c) ref. 23
(d) ref. 24
(e) ref. 25
(f) ref. 26
(g) ref. 27
(h) ref. 28
(i) ref. 29
(j) ref. 30
(k) ref. 31
(l) ref. 32
(m) ref. 33
(n) ref. 4

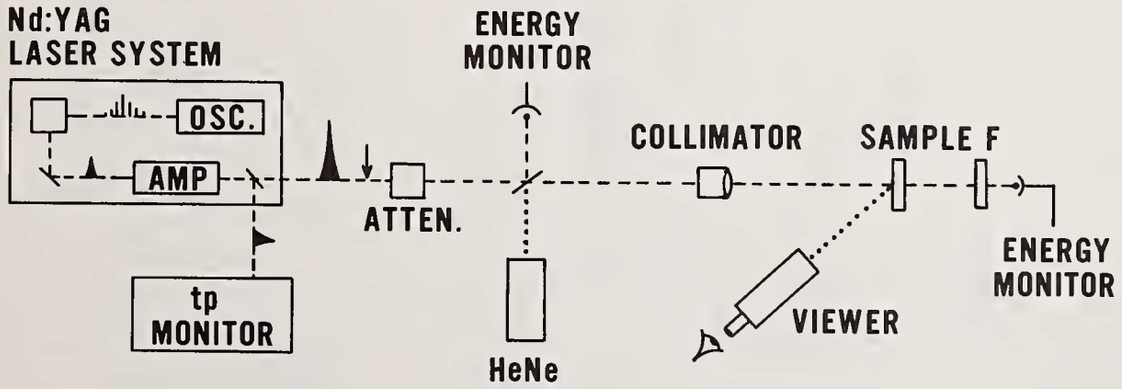

Figure 1. Experimental setup for measuring the two-photon absorption coefficients β_2 at 1.06 μm. The arrow before the beam splitter indicates the position of the second harmonic crystal when 0.53 μm pulses were used.

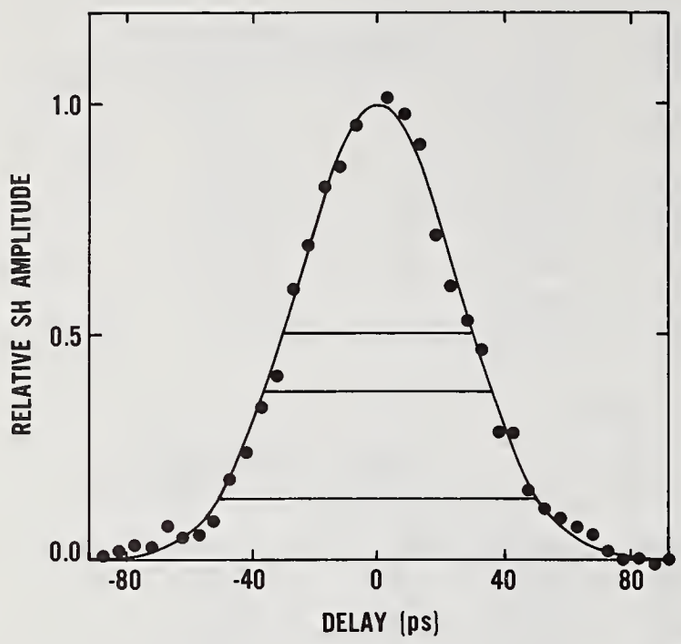

Figure 2. An autocorrelation scan of pulses having a FWHM of 38 psec as calculated from the best fit Gaussian (solid line) autocorrelation.

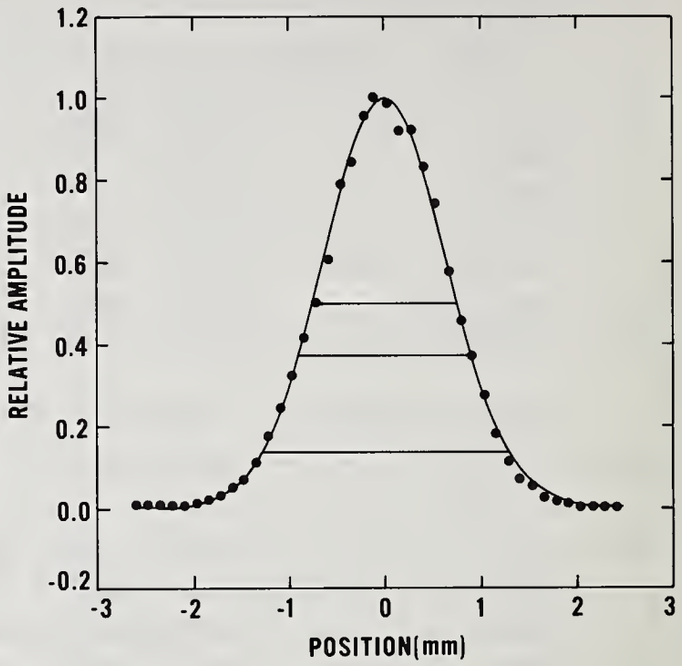

Figure 3. A pinhole beam scan showing a best fit Gaussian (solid line) of FWHM 1.50 mm.

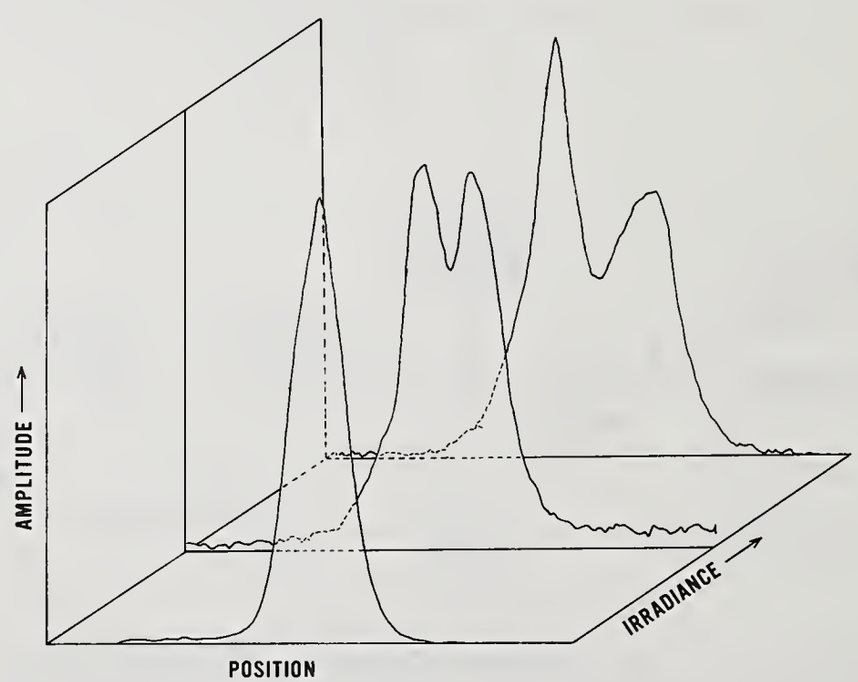

Figure 4. Vidicon scans (equivalent to a pinhole scan) in the near field of the 1.06 μm beam transmitted through a polycrystalline sample of CdTe showing the defocusing for increasing irradiance.

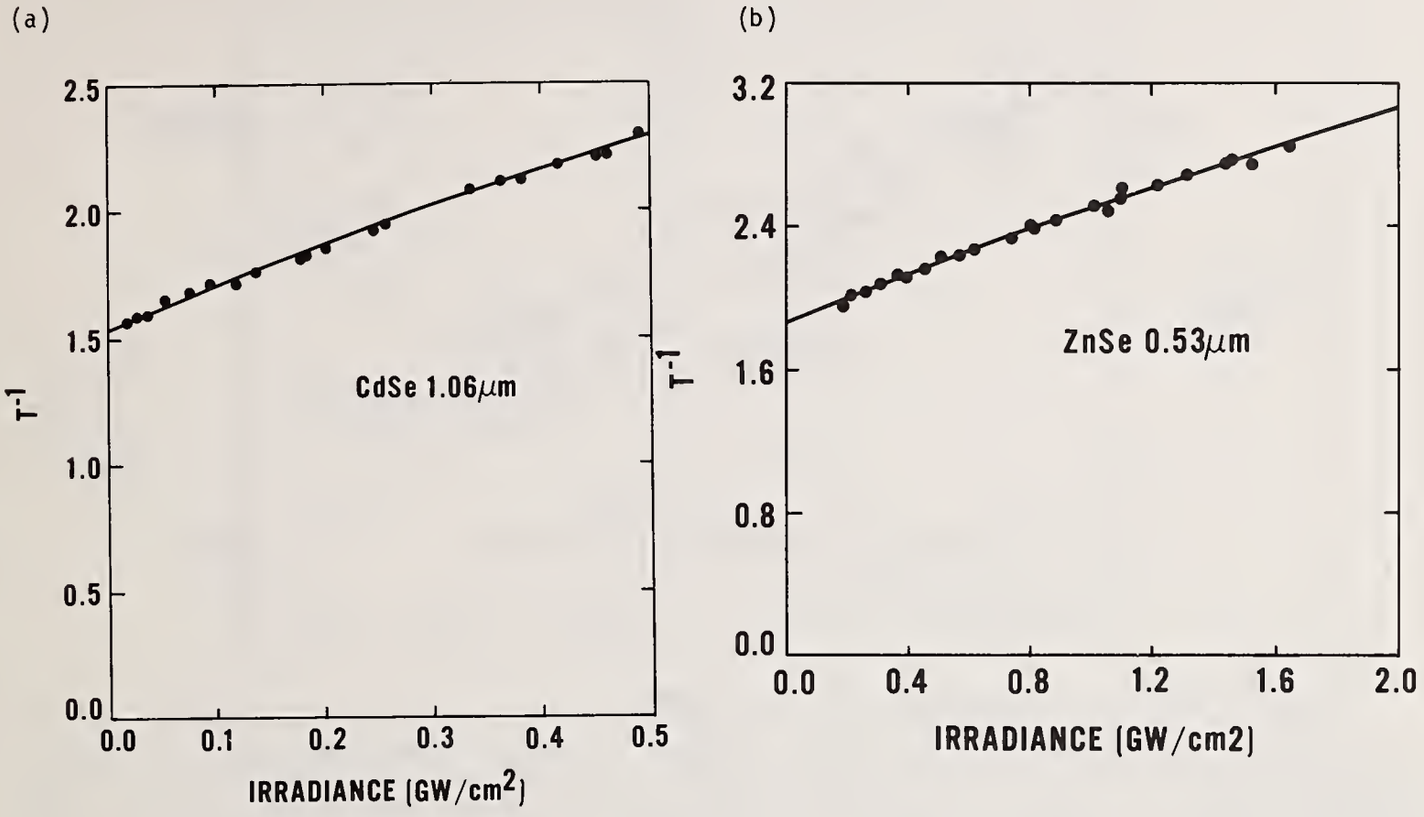

Figure 5. Inverse transmission versus incident irradiance for (a) CdSe at 1.06 μm and (b) ZnSe at 0.53 μm. The solid lines are fits using eq (12) of Section II.

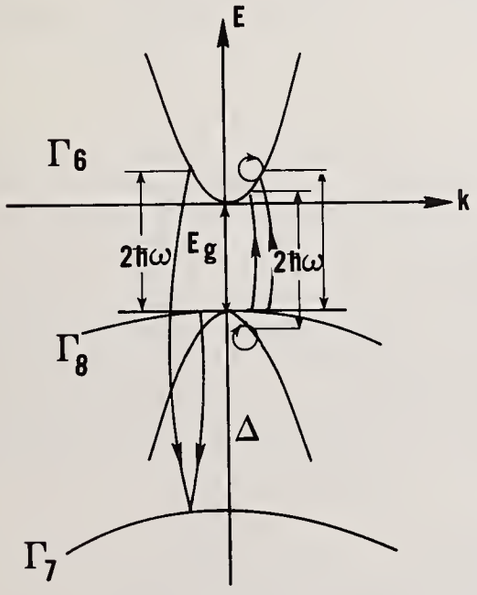

Figure 6. Band structure used in refs. 3 and 4 calculate two-photon absorption coefficients.

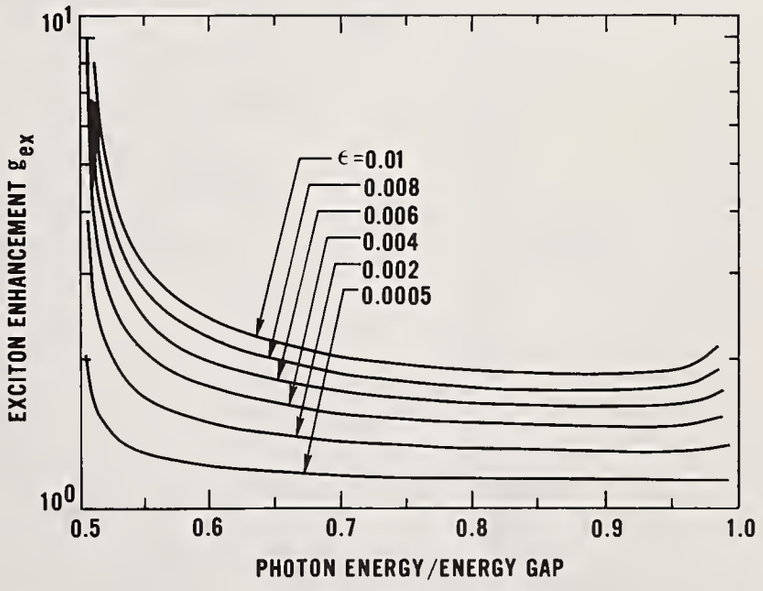

Figure 7. Exciton enhancement factor g_{ex} as a function of $\hbar\omega/E_g$ for various values of the excition binding energy E_b to the band-gap energy E_g (reproduced with permission from ref. 4).

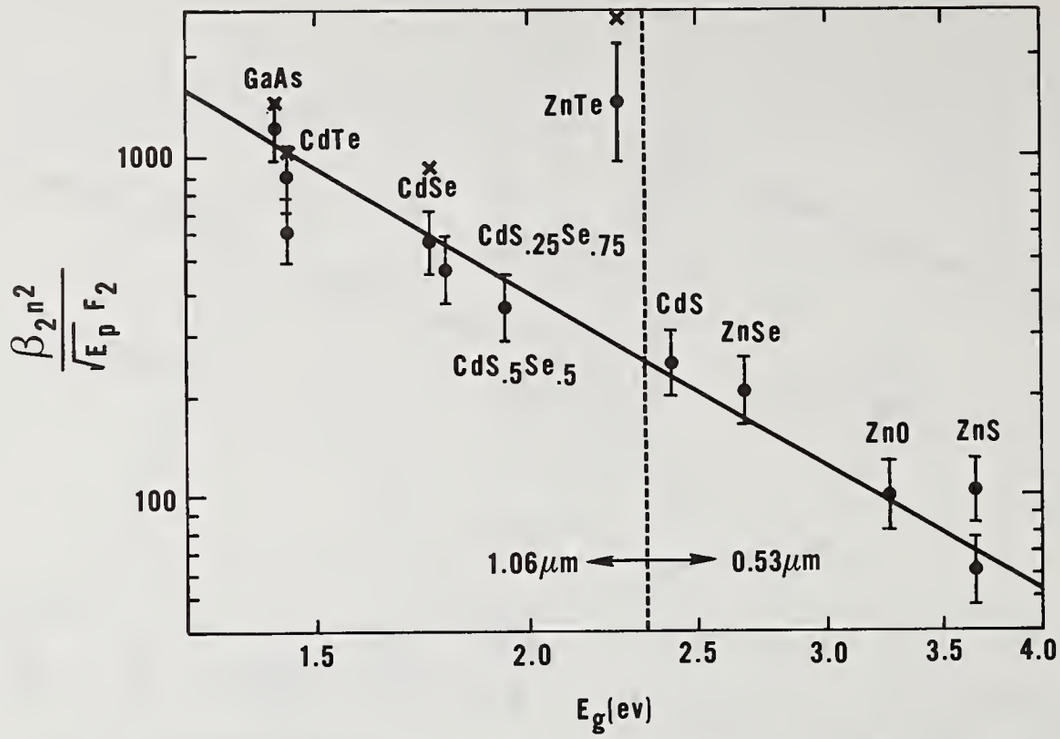

Figure 8. A log-log plot of the scaled two-photon absorption coefficient versus energy gap assuming parabolic band structure. The solid line is a least squares fit of the data to a line of slope -3 (omitting ZnTe). The x's shown for GaAs, CdTe, CdSe and ZnTe are data from ref. 13. Data to the left of the vertical dotted line was taken with 1 μm light, and to the right with 0.5 μm light.

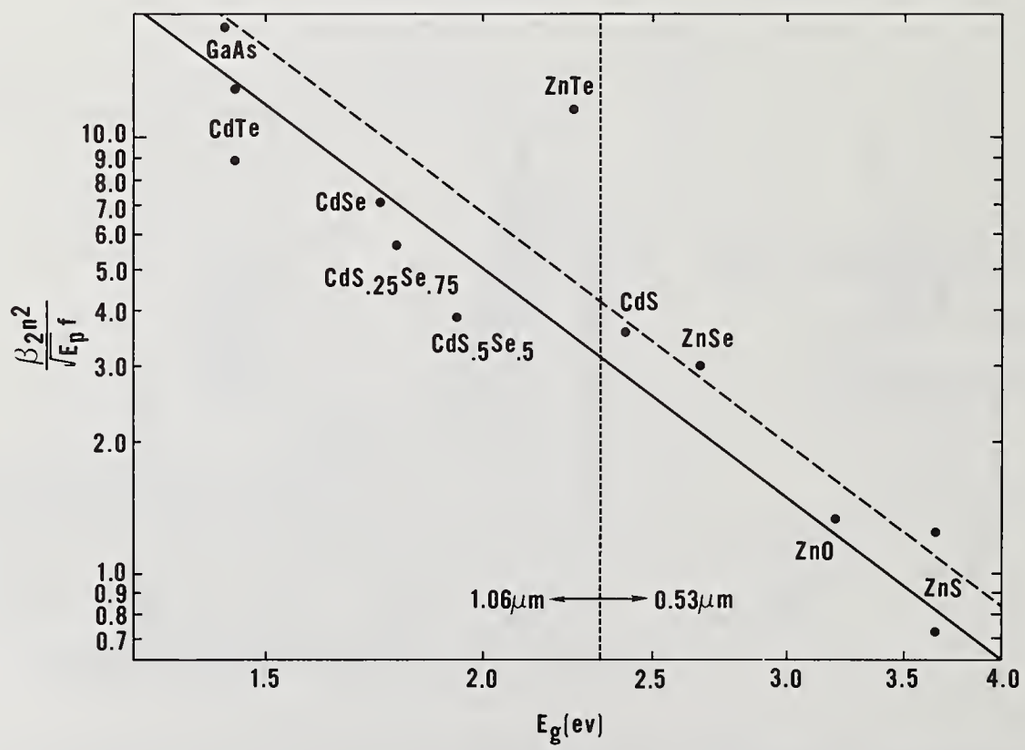

Figure 9. A log-log plot of the scaled two-photon absorption coefficients for nonparabolic band structure ($\Delta << E_g$) versus energy gap. The solid is a least squares fit of the data to a line of slope -3 (omitting ZnTe). The dashed line is the theory of ref. 4.

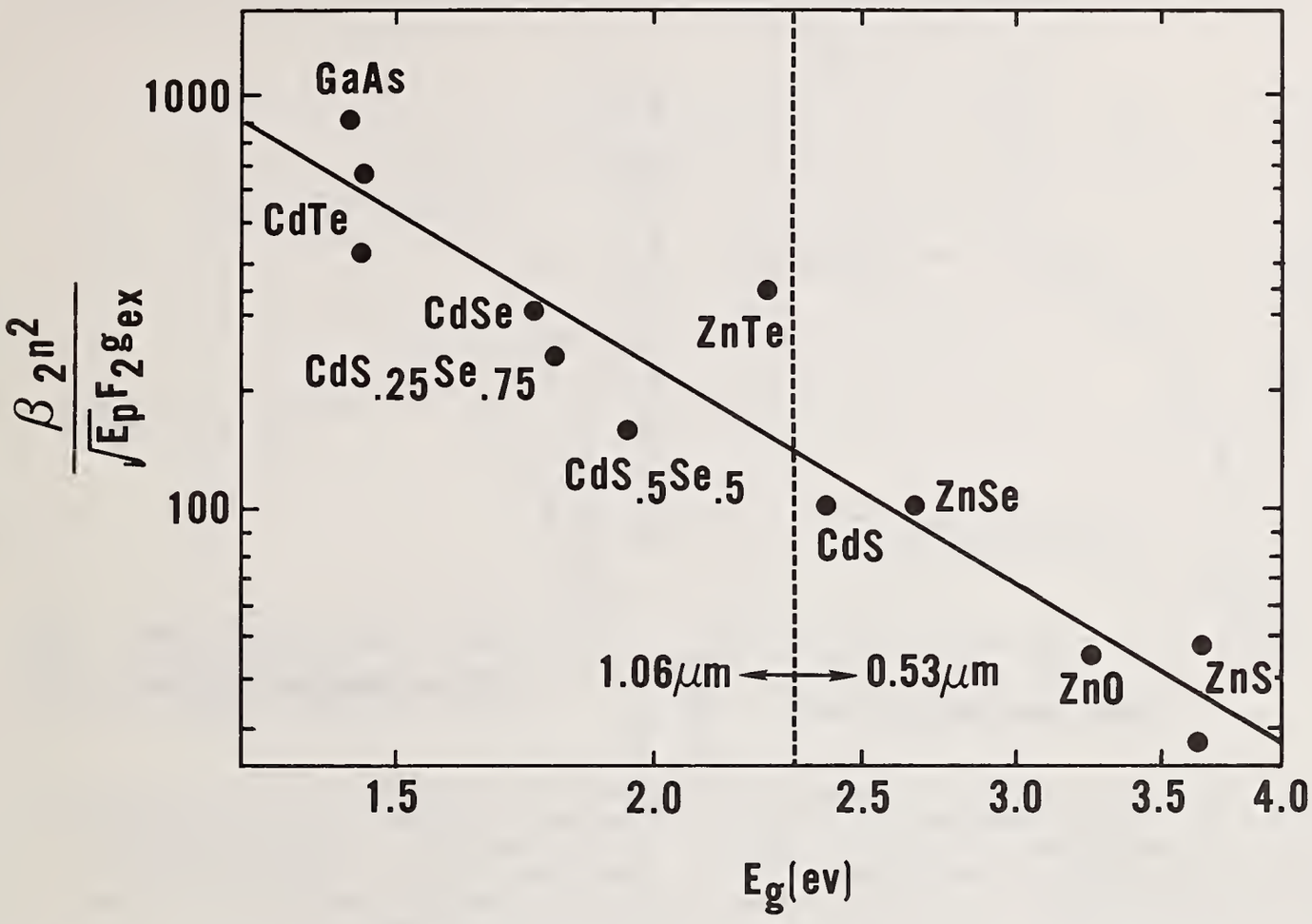

Figure 10. A log-log plot of the scaled two-photon absorption coefficients including exciton enhancement (g_{ex}) for parabolic band structure versus energy gap.

Figure 11. Vidicon scan of the beam transmitted through the polycrystalline sample of CdSe at (a) high irradiance (1 GW/cm^2) and (b) low irradiance (0.3 GW/cm^2) at a distance of 0.5 m behind the sample (near field). The pulsewidth used was 92 psec FWHM. The beam profiles are normalized to have the same on axis fluence. The dashed line is experimental and the solid line is a theoretical fit using eq (16) of Section II.

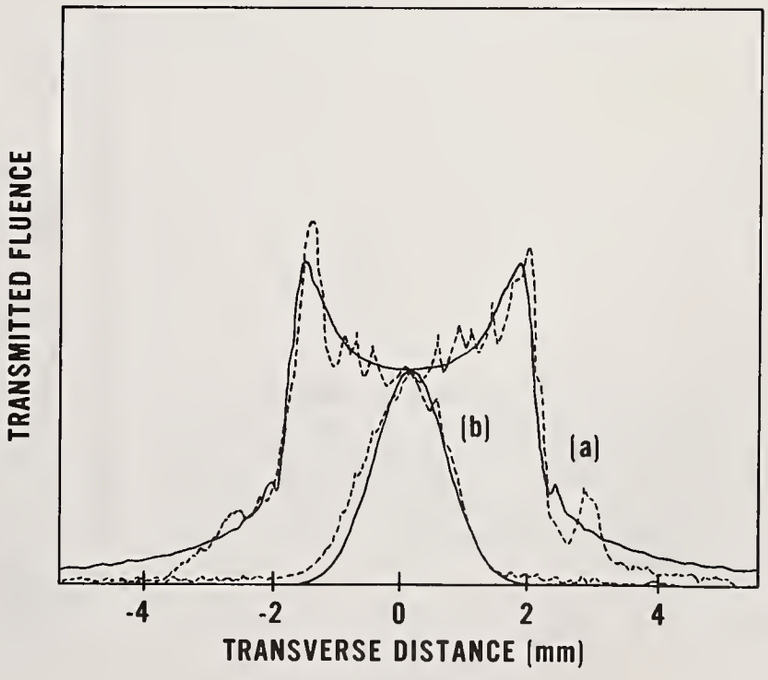

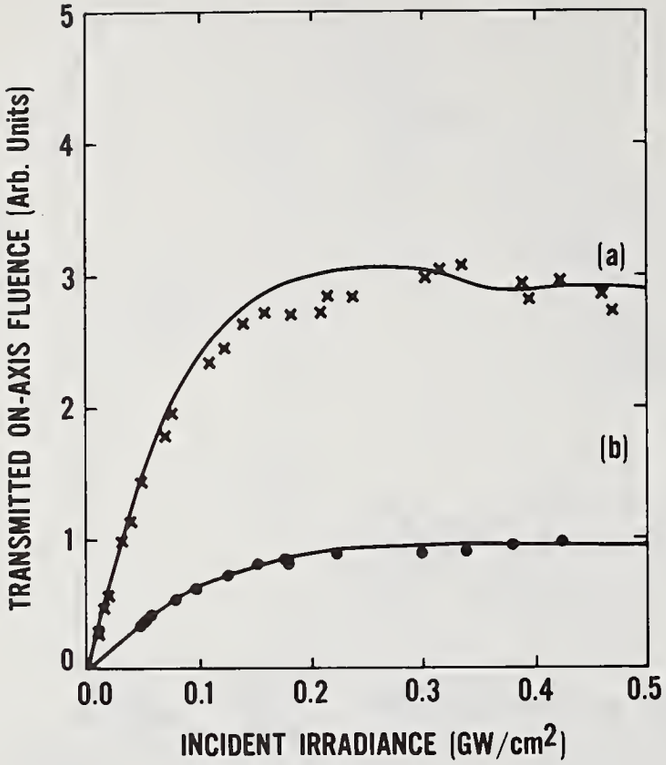

Figure 12. Transmitted on axis fluence as a function of incident irradiance at a distance of 0.5 m behind the sample. (a) 92 psec FWHM pulses and (b) 43 psec FWHM pulses. The solid lines are numerically calculated from eq (16) of Section II.

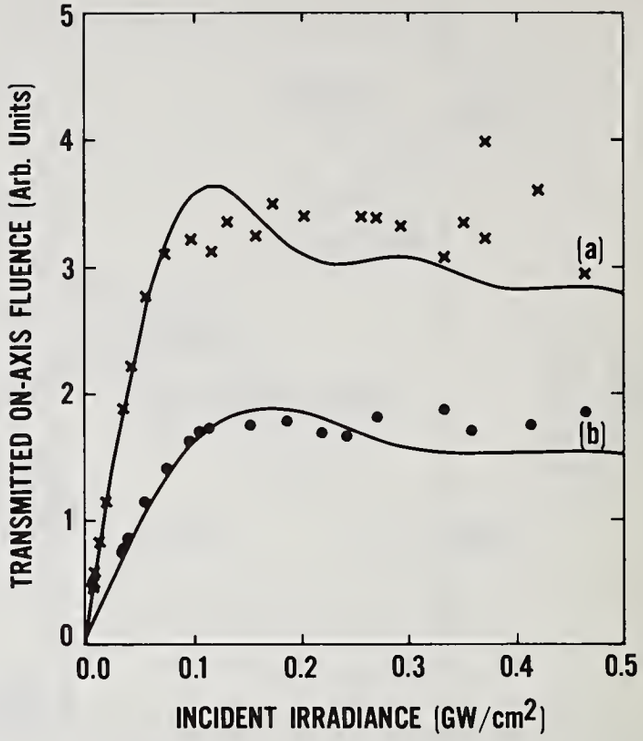

Figure 13. Transmitted on axis fluence as a function of incident irradiance at a distance of 2.0 m behind the sample. (a) 92 psec FWHM pulses and (b) 43 psec FWHM pulses. The solid lines are numerically calculated from eq (16) of Section II.

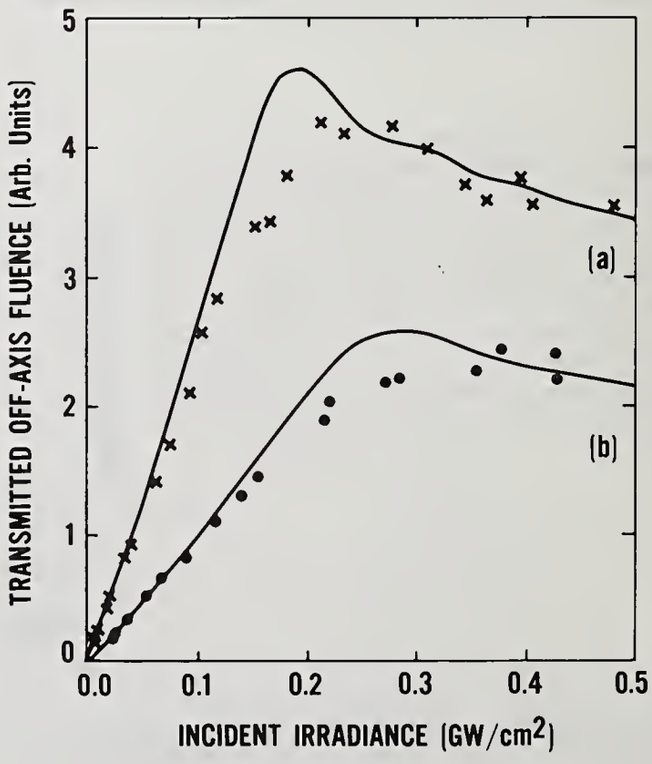

Figure 14. Transmitted fluence measured at a point 1.1 mm off-axis as a function of incident irradiance at a distance of 0.5 m behind the sample. (a) 92 psec FWHM pulses and (b) 43 psec FWHM pulses. The solid lines are numerically calculated from eq (16) of Section II.

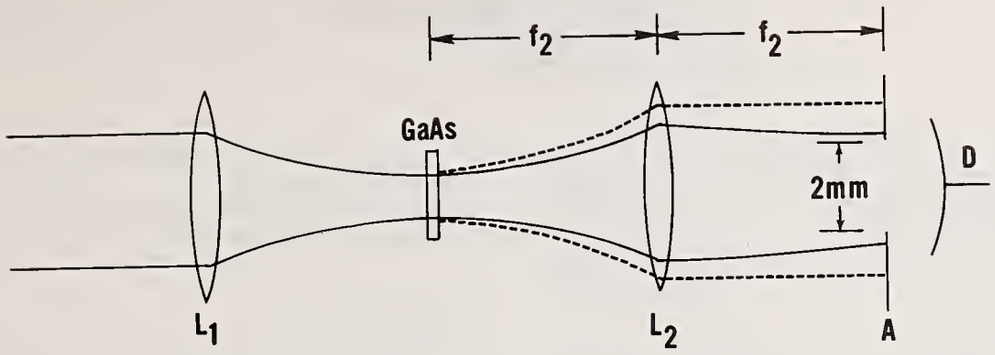

Figure 15. Schematic of GaAs optical limiter.

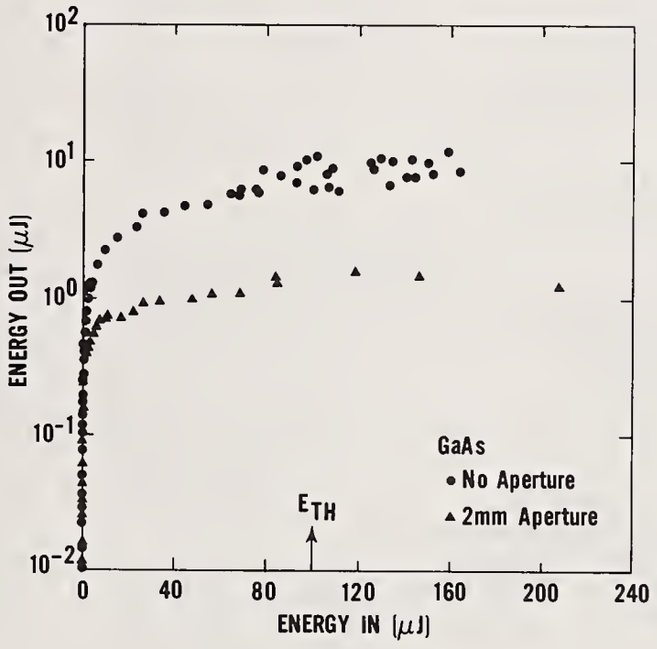

Figure 16. Device response with (triangles) and without (circles) the 2 mm aperture in place. E_{th} represents the single-shot melting threshold.

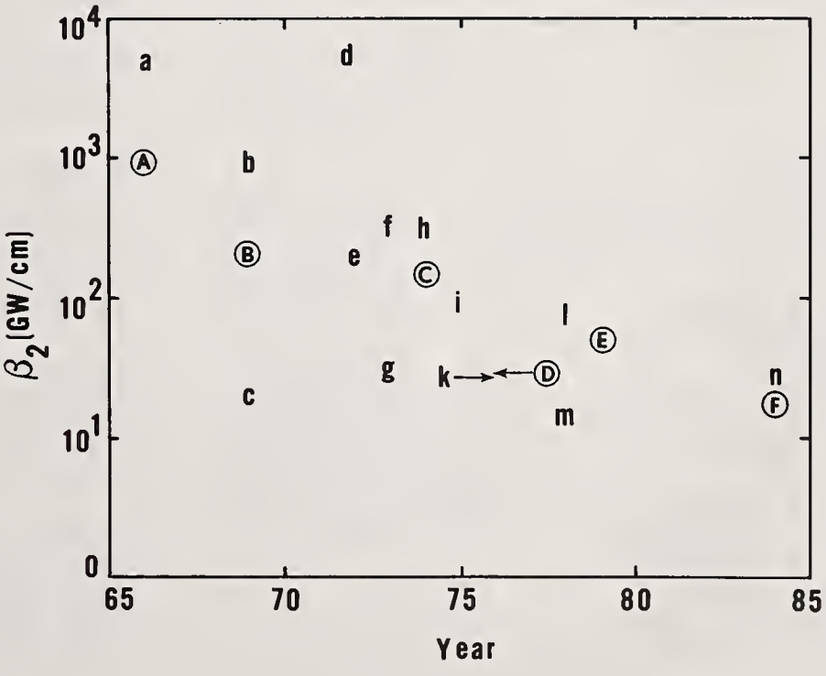

Figure 17. A semilogarithmic plot of the reported two-photon absorption coefficients for GaAs (lower case letters) and CdSe (upper case letters) versus year.

(a)	ref. 36	(A)	ref. 36
(b)	ref. 40	(B)	ref. 39
(c)	ref. 39	(C)	ref. 53
(d)	ref. 46	(D)	ref. 13
(e)	ref. 47	(E)	ref. 54
(f)	ref. 48	(F)	this work
(g)	ref. 49		
(h)	ref. 35		
(i)	ref. 34		
(k)	ref. 13		
(l)	ref. 51		
(m)	ref. 52		
(n)	this work		